Atmos. Meas. Tech., 7, 3705–3715, 2014
www.atmos-meas-tech.net/7/3705/2014/
doi:10.5194/amt-7-3705-2014

Atmospheric Measurement Techniques
Open Access

A Fabry–Perot interferometer-based camera for two-dimensional mapping of SO_2 distributions

J. Kuhn[1], N. Bobrowski[1], P. Lübcke[1], L. Vogel[2], and U. Platt[1]

[1]Institute of Environmental Physics, University of Heidelberg, Heidelberg, Germany
[2]Earth Observation Science, Space Research Centre, University of Leicester, Leicester, UK

Correspondence to: J. Kuhn (jkuhn@iup.uni-heidelberg.de)

Received: 19 January 2014 – Published in Atmos. Meas. Tech. Discuss.: 22 May 2014
Revised: 13 September 2014 – Accepted: 20 September 2014 – Published: 10 November 2014

Abstract. We examine a new imaging method for the remote sensing of volcanic gases, which relies on the regularly spaced narrow-band absorption structures in the UV–VIS of many molecules. A Fabry–Perot interferometer (FPI) is used to compare the scattered sunlight radiance at wavelengths corresponding to absorption bands with the radiance at wavelengths in between the bands, thereby identifying and quantifying the gas. In this first theoretical study, we present sample calculations for the detection of sulfur dioxide (SO_2). Optimum values for the FPI setup parameters are proposed. Furthermore, the performance of the FPI method is compared to SO_2 cameras. We show that camera systems using an FPI are far less influenced by changes in atmospheric radiative transfer (e.g., due to aerosol) and have a great potential as a future technique for examining emissions of SO_2 (or other gases) from volcanic sources and other point sources.

1 Introduction

SO_2 emission rates are routinely measured as a monitoring parameter at many volcanoes (Galle et al., 2010). The chemical lifetime of SO_2, which can account for up to 25 % of the total emitted volcanic gas volume (Textor et al., 2004), is on the order of days, and background concentrations in the ambient atmosphere are usually very low (e.g., McGonigle et al., 2004; Beirle et al., 2014). Therefore, volcanic SO_2 can easily be measured by remote sensing techniques, and it often serves as a dilution tracer when studying the chemistry of more reactive gases emitted by volcanoes (e.g., von Glasow et al., 2009).

Besides COrrelation SPECtroscopy (COSPEC, Moffat and Millan, 1971), differential optical absorption spectroscopy (DOAS, Platt and Stutz, 2008) has become an increasingly more common technique for examining volcanic SO_2 emissions. The DOAS technique allows the application of compact, portable devices, and is furthermore able to measure other gas species (e.g., BrO, OClO, O_3) simultaneously. However, typical DOAS (and COSPEC) measurements provide data only in a single viewing direction. One-dimensional data (e.g., cross sections of volcanic plumes) can be derived by scanning DOAS schemes (e.g., Hönninger et al., 2004; Galle et al., 2010), while two-dimensional data can be acquired by imaging DOAS instruments (Bobrowski et al., 2006; Louban et al., 2009), which are, however, comparably complex and rather slow (with a temporal resolution of about 20 min per image).

The SO_2 camera (Mori and Burton, 2006; Bluth et al., 2007; Kern et al., 2010b; Lübcke et al., 2013) as a non-dispersive device makes use of simplified spectroscopic identification to derive two-dimensional SO_2 column density distributions with a significantly higher temporal resolution (on the order of 1 s per image) than scanning or imaging DOAS instruments. SO_2 is the dominant gaseous absorber in volcanic plumes in the UV wavelength range below 320 nm. Therefore, it is possible to map SO_2 optical density distributions by placing a suitable band-pass filter (full width at half maximum (FWHM) $\approx$ 10 nm, $\sim$ 315 nm center wavelength, usually referred to as "filter A"; see Fig. 1a) in front of a UV-sensitive charge-coupled device (CCD) detector. A second band-pass filter ("filter B") is usually applied to correct for radiative transfer effects of aerosol (e.g., ash, condensates) occurring in the volcanic plume. It is chosen to transmit at

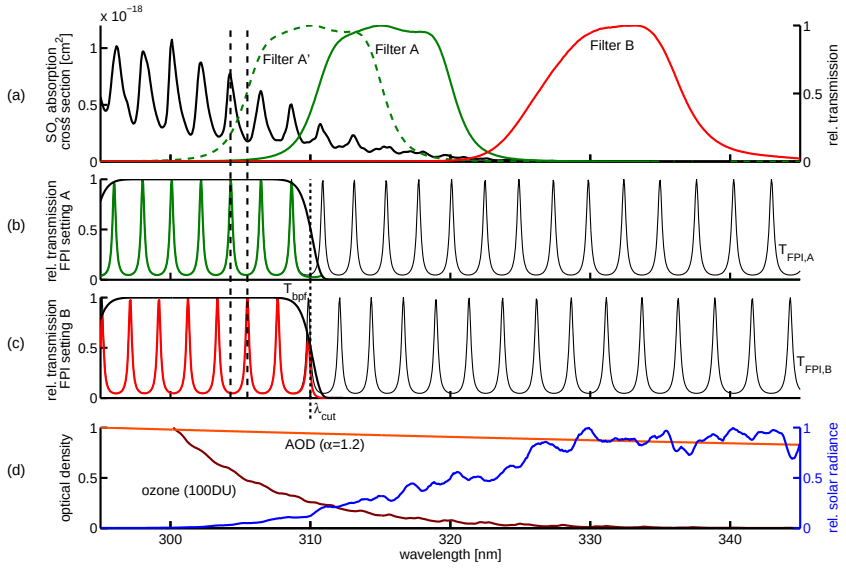

Figure 1. (a) SO_2 absorption cross section (black drawn line, left ordinate axis, data from Bogumil et al., 2003) as a function of wavelength, and transmission curves of filters A, A′ and B (right ordinate axis); **(b)**, **(c)** FPI transmission curve for settings A and B; the dashed vertical lines mark the positions at which FPI transmission maxima coincide with maximum and minimum absorption, respectively. **(d)** Incident solar radiance (blue drawn line, right ordinate axis in relative units), optical density of ozone absorption (100 DU, left ordinate axis) and aerosol extinction (AOD = 1 at 295 nm, Ångström exponent $\alpha = 1.2$, left ordinate axis)

slightly longer wavelength ranges (at about 330 nm), where the SO_2 absorption is much weaker but aerosol impact is approximately the same as for filter A. This technique allows the observation of plume dynamics and measurements of SO_2 emission fluxes on timescales of seconds, which are for instance suitable for investigating correlations between gas emissions and seismic activity at volcanoes (e.g., Nadeau et al., 2011).

However, the rather broadband transmission curve of the filter used in the SO_2 camera encompasses several distinct SO_2 absorption bands, thereby losing spectral information. Moreover, the difference between the center wavelengths of filter A and filter B is relatively high. Hence, wavelength-dependent impacts on the radiation within the plume (e.g., Mie scattering at plume aerosol) can lead to large errors in the measured SO_2 column densities, which are difficult to correct (e.g., Kern et al., 2010a, 2013; Lübcke et al., 2013).

In this paper, a concept for a measurement device combining most of the advantages of DOAS as well as of the SO_2 camera is introduced (Sect. 2). As mentioned already in Kern et al. (2010b), the regularly spaced narrow-band absorption structure of SO_2 allows the measurement of SO_2 by using a Fabry–Perot interferometer (FPI). Radiances at wavelengths of maximum narrow-band SO_2 absorption can be compared to radiances at wavelengths in between these maxima. Thereby, basic limitations of the SO_2 camera technique as mentioned above could be drastically reduced (Sect. 3). The FPI technique introduced here is in general similar to the COSPEC method (Moffat and Millan, 1971; Millan, 2008), which has already been successfully applied at various volcanoes for decades. However, the opto-mechanic system is replaced by interferometer optics, resulting in a smaller, more robust and cost-efficient design, which can record one- or two-dimensional data with high temporal resolution (Sect. 4).

The correlation between the spectral FPI transmission and periodic spectra was first used to study molecular spectra (e.g., Barrett and Myers, 1971). Later, several approaches to identifying and quantifying gases by FPI correlation were reported (mainly in the infrared; see, e.g., Wilson et al., 2007; Vargas-Rodriguez and Rutt, 2009). In contrast to previous studies, this study focuses on UV detection and imaging of volcanic gas emissions.

2 SO_2 camera and FPI measurement principle

The conventional SO_2 camera uses two interference filters (A and B, see Fig. 1a) to compare the scattered sunlight radiances of two neighboring UV wavelength ranges for a certain field of view (FOV, typically around 20°). In the wavelength range of filter A (∼ 310–320 nm, filter transmission curves according to Lübcke et al., 2013), SO_2 is the dominant gaseous absorber in the plume. For each pixel, the radiance measured with filter A in front of the detector is determined by the quantum yield $Q(\lambda)$ of the detector (which is set to unity for this theoretical study), the transmission curve $T_A(\lambda)$ of filter A, and the incident spectral radiance $I_S(\lambda)$:

$$I_A = \int I_S(\lambda) \cdot T_A(\lambda) \cdot Q(\lambda)\, d\lambda \quad (1)$$

I_A is compared to a reference radiance $I_{A,0}$, also measured through filter A:

$$I_{A,0} = \int I_{S,0}(\lambda) \cdot T_A(\lambda) \cdot Q(\lambda)\, d\lambda \quad (2)$$

$I_{S,0}(\lambda)$ is supposed to be the spectral radiance with the radiation not passing through the absorber (the volcanic plume). Since it is generally not possible to measure $I_{A,0}$ with the same viewing direction as I_A, a measurement in a slightly different direction outside the plume is commonly used as an approximation.

Via the Beer–Lambert law, these two radiance values are linked to the optical density τ_A of the volcanic plume for each pixel in the wavelength range of filter A:

$$\tau_A = -\log \frac{I_A}{I_{A,0}} = \tau_{SO_2,A} + \tau_{other,A}, \quad (3)$$

with

$$\tau_{SO_2,A} = \overline{\sigma}_{SO_2,A} \cdot S_{SO_2}. \quad (4)$$

The plume optical density τ_A in the wavelength window of filter A is a function of the SO_2 absorption $\tau_{SO_2,A}$ and the contribution of other extinction effects $\tau_{other,A}$ (e.g., scattering at plume aerosol). $\overline{\sigma}_{SO_2,A}$ is the weighted absorption cross section of SO_2 averaged over the wavelength range of filter A. S_{SO_2} is the SO_2 column density.

In an analogous way, τ_B is the optical density measured through filter B ($\sim$ 325–340 nm), where the SO_2 absorption is significantly smaller (see Fig. 1a):

$$\tau_B = -\log \frac{I_B}{I_{B,0}} = \tau_{SO_2,B} + \tau_{other,B}. \quad (5)$$

The optical density τ_B is subtracted from τ_A in order to obtain a signal that only depends on SO_2 absorption. This correction assumes that all extinction originating from effects other than SO_2 absorption are broadband (approximately independent of wavelength in the regarded spectral range; i.e., $\tau_{other,A} \approx \tau_{other,B}$):

$$\tilde{\tau} = AA = \tau_A - \tau_B \approx \tau_{SO_2,A} - \tau_{SO_2,B} = \left(\overline{\sigma}_{SO_2,A} - \overline{\sigma}_{SO_2,B}\right) \cdot S_{SO_2}. \quad (6)$$

$\tilde{\tau}$ is called apparent absorbance (AA), and ideally is proportional to S_{SO_2}. The weighted SO_2 absorption cross sections ($\overline{\sigma}_{SO_2,A}, \overline{\sigma}_{SO_2,B}$) can be determined using calibration cells (e.g., Mori and Burton, 2006). Another possible calibration method for the SO_2 camera is to use additional DOAS measurements (e.g., Lübcke et al., 2013).

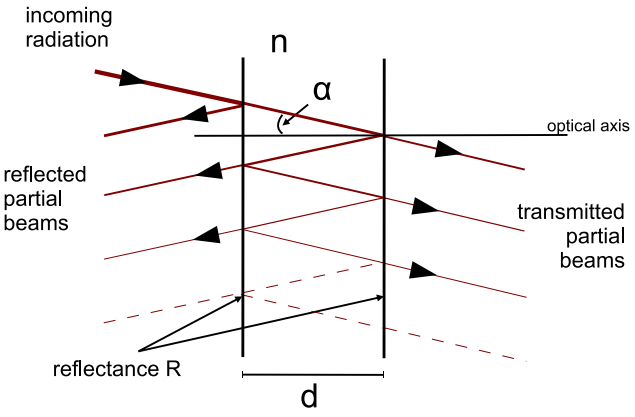

Figure 2. Fabry–Perot interferometer: incoming radiation undergoes multiple reflections between two plane-parallel surfaces of reflectance R, mounted at distance d. Interference of the transmitted partial beams leads to the transmission structure (see Eq. 8, Fig. 1), which can be optimized to match periodic absorption structure.

By using an FPI in our new proposed instrument, more detailed spectral information is taken into account, allowing a higher SO_2 sensitivity to be reached. Moreover, interferences of the SO_2 measurement with radiative transfer effects such as wavelength-dependent (aerosol) extinction and changing ozone background are reduced.

An FPI consists of two plane-parallel surfaces with reflectance R at separation d (see Fig. 2). Incident radiation is split up into a reflected and a transmitted part at the individual surfaces. The partial beams pass through different optical path lengths between the two surfaces before leaving the FPI. For radiation of wavelength λ and a refractive index n of the medium between the surfaces, this results in a phase difference

$$\delta(\lambda; n, d, \alpha) = 2\pi \cdot \frac{2nd}{\lambda} \cdot \cos\alpha \quad (7)$$

between two consecutively transmitted (or reflected) partial beams. α is the angle between the propagation direction of the partial beams and the surface normal in between the two surfaces. The reflectance R of the surfaces determines the finesse (F) (see Eq. 10) of the FPI. F is a measure of the number of partial beams, which effectively interfere with each other after being transmitted (or reflected) by the FPI ($F(R)$ increases monotonically). Superposition of all transmitted partial beams with their respective phase shifts and neglect of absorption effects yield the transmission profile of the FPI (Perot and Fabry, 1899):

$$T_{FPI}(\lambda; d, n, \alpha, R) = \left[1 + C_F \cdot \sin^2\left(\frac{\delta(\lambda)}{2}\right)\right]^{-1} \quad (8)$$

$$= \left[1 + C_F \cdot \sin^2\left(\frac{2nd\pi}{\lambda}\cos\alpha\right)\right]^{-1}, \quad (9)$$

with

$$C_F = \frac{4R}{(1-R)^2} \approx \frac{4 \cdot F^2}{\pi^2} \quad \text{or} \quad F \approx \frac{\pi\sqrt{R}}{1-R}. \tag{10}$$

The approximation for F in Eq. (10) is only valid for $R > 0.5$. T_{FPI} is a periodic function of δ, with maxima for δ attaining integer multiples of 2π. For an increasing finesse coefficient C_F and thus for increasing F or R, the spectral transmission maxima get sharper.

The periodic, comb-shaped transmission structure of the FPI can be used to compare the radiance transmitted at wavelengths corresponding to the narrow-band SO_2 absorption maxima with those corresponding to absorption minima by using appropriate FPI instrument parameters. In the simplest case, two FPI settings are used. In one FPI setting (setting A, Fig. 1b and c), the parameters are chosen such that the transmission maxima of the FPI coincide with the maxima of the absorption structure of SO_2. In another setting (setting B), the transmission maxima of the FPI coincide with the minima of the SO_2 absorption structure. Setting B is reached by changing δ. By comparing the transmitted radiances recorded with FPI settings A and B, the SO_2 column density can be derived by calibration, similarly to the SO_2 camera and COSPEC.

However, scattered solar radiation at wavelength ranges without a narrow-band SO_2 absorption structure matching the FPI transmission has to be excluded. Towards shorter wavelengths with a strong narrow-band absorption structure, the scattered solar radiance at ground level decreases very quickly (mostly because of increasing absorption due to stratospheric ozone). For FPI SO_2 measurements in the regarded spectral range, it is therefore sufficient to prevent measurements at longer wavelengths, where the SO_2 absorption structure is weak. This can be accomplished by a superimposed short-pass or band-pass interference filter (bpf) with transmission T_{bpf} (see Fig. 1b and c), which will be characterized by the largest transmitted wavelength λ_{cut}.

The radiance measured by the detector after having traversed the band-pass filter and the FPI in the setting i = A, B is given by (compare Eq. 1)

$$I_{\mathrm{FPI},\,i} = \int I_{\mathrm{S}}(\lambda) \cdot T_{\mathrm{FPI},\,i}(\lambda) \cdot T_{\mathrm{bpf}}(\lambda) \cdot Q(\lambda)\mathrm{d}\lambda. \tag{11}$$

By comparison to reference measurements

$$I_{0,\mathrm{FPI},\,i} = \int I_{\mathrm{S},\,0}(\lambda) \cdot T_{\mathrm{FPI},\,i}(\lambda) \cdot T_{\mathrm{bpf}}(\lambda) \cdot Q(\lambda)\mathrm{d}\lambda, \tag{12}$$

the optical densities for the corresponding FPI transmissions are determined:

$$\tau_{\mathrm{FPI},\,i} = -\log \frac{I_{\mathrm{FPI},\,i}}{I_{0,\,\mathrm{FPI},\,i}} = \tau_{\mathrm{SO_2,\,FPI},\,i} + \tau_{\mathrm{other,\,FPI},\,i}. \tag{13}$$

$\tau_{\mathrm{SO_2,\,FPI},\,i}$ is the part of the SO_2 absorption $\tau_{\mathrm{SO_2}}$ seen through the transmission profile of the respective FPI setting and therefore proportional to $S_{\mathrm{SO_2}}$. When choosing settings A and B as described above, $\tau_{\mathrm{SO_2,\,FPI,\,A}}$ and $\tau_{\mathrm{SO_2,\,FPI,\,B}}$ differ in the presence of SO_2, while $\tau_{\mathrm{other,\,FPI},\,i}$ is considered to be approximately the same for the two FPI settings. Similarly to the SO_2 camera, we get

$$\tilde{\tau}_{\mathrm{FPI}} = \mathrm{AA_{FPI}} = \tau_{\mathrm{FPI,\,A}} - \tau_{\mathrm{FPI,\,B}} \propto \tau_{\mathrm{SO_2}} \propto S_{\mathrm{SO_2}} \tag{14}$$

The crucial difference to the SO_2 camera measurement is that instead of comparing the radiances of two separate spectral ranges averaged over an FWHM of ~ 10 nm, relative changes in the narrow-band absorption structure are now taken into account. Since the transmission structures of FPI settings A and B are interleaved and differ by a shift of only about 1 nm, the approximately broadband, non-SO_2 contributions of $\tau_{\mathrm{other,\,FPI,\,A}}$ and $\tau_{\mathrm{other,\,FPI,\,B}}$ cancel each other out more efficiently. $\mathrm{AA_{FPI}}$ is therefore much less susceptible to wavelength-dependent effects like, e.g., aerosol extinction.

Characteristics of an SO_2 FPI device

In the following, the dependency of $\mathrm{AA_{FPI}}$ on certain key parameters, like the finesse F of the FPI, the surface separation d or the incidence angle α of incoming radiation, is discussed.

To examine the characteristics of an FPI measurement as described above, the incoming spectral radiance $I_{\mathrm{S}}(\lambda)$ of scattered solar radiation, having traversed the volcanic plume, is calculated according to the approximation of the Beer–Lambert law:

$$I_{\mathrm{S}}(\lambda) = I_{\mathrm{S},\,0}(\lambda) \cdot e^{-\tau(\lambda)} = I_{\mathrm{S},\,0}(\lambda) \cdot e^{-\sigma_{\mathrm{SO_2}}(\lambda) \cdot S_{\mathrm{SO_2}}} \tag{15}$$

For the moment, the SO_2 absorption is assumed to be the only extinction effect on the radiation traversing the plume. The absorption cross section $\sigma_{\mathrm{SO_2}}(\lambda)$ of Bogumil et al. (2003) for 293 K was used (see Fig. 1). As the reference radiance $I_{S,0}(\lambda)$, a measured spectrum of scattered sunlight was employed. A modified Gaussian profile was used to model the spectral transmission $T_{\mathrm{bpf}}(\lambda)$ of the band-pass filter (see Fig. 1):

$$T_{\mathrm{bpf}}(\lambda) = A \cdot \exp\left[-0.5\left(\frac{|\lambda - \lambda_{\mathrm{c}}|}{\sigma}\right)^{\gamma}\right] \tag{16}$$

The center wavelength λ_{c} determines λ_{cut}, while $A = 0.65$ and $\gamma = 2 \cdot \sigma = 15.2$ constitute constant shape parameters of the transmission profile, which was matched to a real band-pass interference filter transmission curve.

The integrated radiances $I_{\mathrm{FPI},\,i}$ and $I_{0,\,\mathrm{FPI},\,i}$ arriving at the detector can be calculated using $I_{\mathrm{S},\,0}(\lambda)$ and $I_{\mathrm{S}}(\lambda)$ (Eq. 15) multiplied by the transmission curves for the FPI (Eq. 8) and the band-pass filter (Eq. 16).

When using an FPI to measure SO_2 in the above-described way, certain points have to be considered. In principle, changing δ leads to both a shift and a stretch of the spectral FPI transmission. However, once the order m of an observed transmission maximum at wavelength λ_m of the FPI

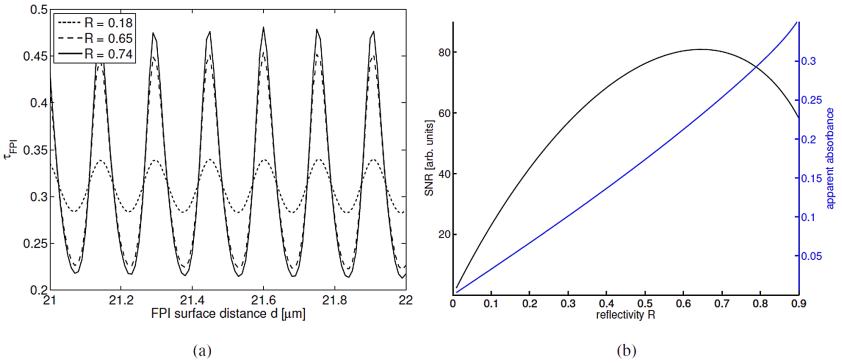

(a) (b)

Figure 3. (a) Optical density τ for an SO_2 slant column density $S_{SO_2} = 10^{18}$ molec cm^{-2} observed by an FPI setup for varying distance d between the surfaces, calculated for FPI reflectivities of 0.18, 0.65 and 0.74. The difference in the optical densities recorded at maximum (d_A at, e.g., 21.6 µm) and minimum (d_B) values is the apparent absorbance. **(b)** The apparent absorbance (blue line) grows monotonically with the reflectivity R. However, for high R (and thus for high F), the SNR is decreasing, since less radiation is transmitted.

is high enough, small changes in δ (Eq. 7) lead in a good approximation only to a wavelength shift of the transmission curve, while the stretch can be neglected ($\frac{\text{shift}}{\text{stretch}} = m + 1$). For an FPI transmission profile, which is matched to the SO_2 absorption cross section in the spectral range of interest (see Fig. 1), the order of the maxima is about $m = \frac{2nd}{\lambda_m} \approx 140$. Therefore, the change between FPI settings A (transmission maxima on SO_2 absorption bands) and B (transmission maxima between SO_2 absorption bands) can easily be realized by a small change in d, n or $\cos\alpha$.

In the following examination, we assume that only the surface separation d of the FPI is varied for normal incident radiation ($\alpha = 0$) and $n = n_{air}$. Figure 3a shows the modeled optical density τ_{FPI}, measured by an FPI device as a function of d for FPI surface reflectivities of 0.18, 0.65 and 0.74. An SO_2 slant column density of $S_{SO_2} = 10^{18}$ molec cm^{-2} (400 ppmm, at standard pressure and 20 °C) was assumed, which is a common value measured at volcanic plumes. The oscillating behavior of $\tau_{FPI}(d)$ mirrors the FPI transmission structure being shifted along the wavelength axis across the narrow-band absorption structure of SO_2. FPI surface separations d corresponding to a maximum optical density (i.e., the FPI transmission maxima coincide with the SO_2 absorption bands) suggest values for d_A in setting A (e.g., 21.6 µm). The change $d_{AB} = d_B - d_A$ in the FPI surface separation required to reach setting B (minimum optical density, i.e., FPI transmission maxima in between SO_2 absorption bands) would be around 80 nm (for the adjoining minimum).

The modulation of τ_{FPI} as a function of d (Fig. 3a) increases with the reflectivity R (and thus with the finesse F), since the transmission maxima get sharper, and therefore only radiation most affected by SO_2 absorption is transmitted. However, a higher finesse must be weighted against the reduced integrated transmission of the FPI, i.e., reduced radiation throughput. Since less radiation arrives at the detector, the signal-to-noise ratio SNR $= \frac{AA_{FPI}}{\Delta AA_{FPI}}$ starts to decrease again at values of R exceeding about 0.65, while AA_{FPI} increases monotonically (see Fig. 3b).

Table 1. Result of the numerical optimization of the SNR of an FPI SO_2 measurement for $S_{SO_2} = 10^{18}$ molec cm^{-2}; d_A is the separation of the surfaces in FPI setting A, d_{AB} the change in surface separation to get from FPI setting A to FPI setting B, F the finesse and λ_{cut} the cutoff wavelength of the band-pass filter towards longer wavelengths.

Parameter	Maximizing value
d_A	21.6 µm
d_{AB}	84 nm
R	0.65 ($F = 7.1$)
λ_{cut}	310 nm

A similar compromise has to be made when choosing the cutoff wavelength λ_{cut}. The SO_2 absorption structure vanishes towards longer wavelengths, while the scattered solar radiance increases. Hence, there is also a certain value for λ_{cut} optimizing the SNR.

In order to be able to assess the noise ΔAA_{FPI} of a hypothetical instrument, we assumed $I_{FPI,i}$ and $I_{0,FPI,i}$ to be proportional to the number of photons reaching a hypothetical detector. Photon statistics then imply that the measurement error of the radiance is given by $\Delta I \propto \sqrt{I}$ and that the error in AA_{FPI}, ΔAA_{FPI} can be determined via Gaussian error propagation. The absolute value of the SNR is still dependent on the absolute radiances reaching the detector, which we do not know yet. Thus, in this theoretical study, SNR is used as a value proportional to the real SNR, which is sufficient for our optimization problems.

In order to find optimal parameters of an FPI setup for normal incidence of radiation on the FPI ($\alpha = 0$), the SNR was optimized numerically. Table 1 shows the varied setup parameters and their values maximizing the SNR for an SO_2 column density of $S_{SO_2} = 10^{18}$ molec cm^{-2}.

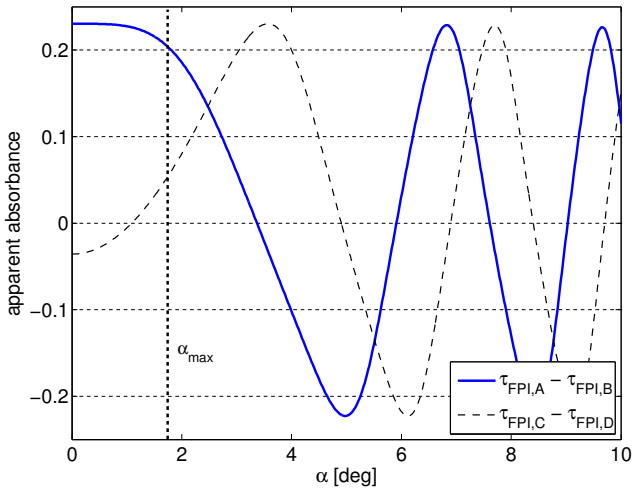

Figure 4. AA_{FPI} as a function of the incident illumination angle α for an SO_2 slant column density of $S_{SO_2} = 10^{18}$ molec cm^{-2} (blue drawn line): small changes in $\cos\alpha$ cause a shift of T_{FPI} in wavelength, which leads to an oscillating progression of AA_{FPI} over α. $\alpha_{max} \approx 1.8°$ limits the range of angles for the assumption of parallel incident radiation. The dashed line shows a measurement with two different FPI surface separations ($d_C = d_A + \frac{1}{2}d_{AB}$ and $d_D = d_A + \frac{3}{2}d_{AB}$). By using more than two FPI settings, the sensitivity for arbitrary incidence angles can be obtained (see Sect. 4).

Since δ is proportional to $\cos\alpha$ (Eq. 7), a small change in $\cos\alpha$ also causes a spectral shift in the FPI transmission structure T_{FPI}. Figure 4 shows the dependency of AA_{FPI} on α for the above-proposed FPI setup and for $S_{SO_2} = 10^{18}$ molec cm^{-2} (blue drawn line). The behavior is approximately flat until reaching $\alpha_{max} \approx 1.8°$, which constitutes a limitation for the imaging instrument setups described below (see Sect. 4). For higher values of α, the apparent absorbance AA_{FPI} oscillates between negative ($\tau_{FPI,A} < \tau_{FPI,B}$) and positive extrema, attaining FPI incident angles α with vanishing AA_{FPI} in between them. Since the FPI transmission structures of the two settings (A and B) are shifted in the same way across several SO_2 absorption bands, both positive and negative values of AA_{FPI} carry the same SO_2 information. AA_{FPI} can thus be redefined as $|AA_{FPI}|$.

3 Comparison to conventional SO_2 cameras

The measurement principle as described up to now, could, e.g., be used to construct a simple "one-pixel" (OP) FPI SO_2 detector with a rather narrow FOV. Such an instrument would indeed make sense, since it would have a sensitivity and selectivity comparable to a spectrometer (as, e.g., used in the Network of Observation of Volcanic and Atmospheric Change (NOVAC); see Galle et al., 2010), but could potentially be a more compact and more economic alternative. Likewise, the measurement principle of the filter-based SO_2 camera could be adopted for an OP instrument. In the following, we compare the performance of an OP FPI device with a hypothetical OP SO_2 "camera". The conclusions drawn are also relevant for two-dimensional (2-D) cameras, i.e., 2-D SO_2 cameras and 2-D FPI cameras as described in Sect. 4.

An FPI instrument with the parameters of Table 1 was considered; transmission curves of the corresponding settings are shown in Fig. 1. For the SO_2 camera, the filter curves of Lübcke et al. (2013) were applied (see also Fig. 1). Moreover, a second SO_2 camera setup with filter A shifted by 5 nm towards shorter wavelengths is additionally examined for comparison to represent different popular setups of SO_2 cameras. In the following, the shifted filter A is called filter A′.

3.1 Sensitivity to SO_2 and interference due to Mie scattering

Figure 5a shows the AA for the respective measurement method as a function of the SO_2 column density S_{SO_2}. In order to examine the plume aerosol impact on the AA, two calibration curves were simulated for each device. The solid lines show the AA with SO_2 absorption being the only effect on $I_{S,0}(\lambda)$ (see Eq. 15). For the second set of lines (dashed), an additional wavelength-dependent extinction $\tau_{aerosol}(\lambda)$ from a Mie scattering aerosol was assumed using an Ångström exponent of 1.2, which was found to be representative for volcanic plumes (Spinetti and Buongiorno, 2007). The wavelength dependency of the aerosol extinction is then described by

$$\tau_{aerosol}(\lambda) = \tau_{aerosol,\lambda_0} \cdot \left(\frac{\lambda}{\lambda_0}\right)^{-1.2}. \quad (17)$$

The aerosol optical density (AOD) was fixed to $\tau_{aerosol,\lambda_0} = 1$ at $\lambda_0 = 295$ nm, which corresponds to a rather low AOD of a volcanic plume (Fig. 1d).

The SO_2 camera with filter A′ is more sensitive to SO_2 absorption, since $\overline{\sigma}_{SO_2,A'}$ is greater than $\overline{\sigma}_{SO_2,A}$ (see Fig. 1 and Eq. 4). However, the increase in sensitivity goes together with a decrease in incoming solar radiance at shorter wavelengths.

The wavelength-dependent AOD causes a higher extinction in the spectral ranges of filters A and A′ than in the spectral range of filter B ($\tau_{aerosol,A} > \tau_{aerosol,B}$), leading to an offset ΔAA_{AOD} towards higher AA for the respective SO_2 camera setups. For $S_{SO_2} = 10^{18}$ molec cm^{-2}, the assumed, small amount of aerosol thus accounts for relative deviations of $\frac{\Delta AA_{AOD}}{AA} \approx 54\,\%$ when using filter A, and $\frac{\Delta AA_{AOD}}{AA} \approx 38\,\%$ when using filter A′. The smaller relative deviation for filter A′ results from the different wavelength dependencies of aerosol extinction and SO_2 absorption.

The FPI device (drawn black line in Fig. 5a) is more sensitive to SO_2 than either of the two filter-based setups. This is because narrow-band changes in the SO_2 absorption cross section below 310 nm are larger than the averaged cross sections $\overline{\sigma}_{SO_2,A'}$ and $\overline{\sigma}_{SO_2,A}$, respectively. For increasing S_{SO_2},

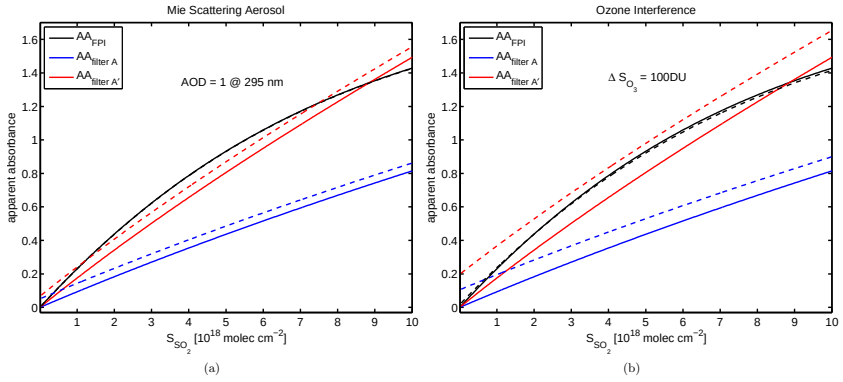

Figure 5. Modeled calibration curves (without aerosol) for the OP FPI SO_2 device (black drawn line, flattening for high S_{SO_2} due to saturation) and the OP filter-based SO_2 devices with filter A (blue drawn line) and filter A′ (red drawn line); **(a)** deviation (dashed lines) due to Mie scattering aerosol with an optical density (AOD) of 1 at 295 nm. The filter-based SO_2 devices (regardless of the filter used) show a considerable false positive SO_2 signal, while the curve for the FPI device hardly separates from the undisturbed calibration curve. **(b)** Deviation due to ozone interference, where a change in $\Delta S_{O_3} = 100$ DU was assumed. Again, the FPI measurement shows far less deviation.

the progression of AA_{FPI} gradually flattens, since saturation effects at wavelengths of strong SO_2 absorption bands occur. We ran the simulation to SO_2 column densities of up to 10^{19} molec cm^{-2}, a value that may only be observed close to the volcanic vent of very strong SO_2 emitters. The saturation only leads to a reduced sensitivity for very high SO_2 absorptions, and may be dealt with by carefully calibrating the FPI device.

While a saturation effect can be observed, we also see that there is hardly any sensitivity to the added amount of aerosol ($\frac{\Delta AA_{FPI,\,AOD}}{AA_{FPI}} < 1\,\%$ for $S_{SO_2} = 10^{18}$ molec cm^{-2}); in fact, the dashed black line is almost completely covered by the drawn black line, meaning that $\tau_{aerosol,\,FPI,\,A} \approx \tau_{aerosol,\,FPI,\,B}$ still holds for the chosen FPI settings.

Note that in this simple calculation, we only considered aerosol extinction. This approximation holds for low plume AOD. Radiative transfer effects like light dilution and multiple scattering in the plume (e.g., Kern et al., 2010a; Millan, 1980) will still affect the FPI method in a manner similar to almost all passive UV absorption measurements. The FPI approach only removes errors of the traditional SO_2 camera introduced by measuring at different wavelength ranges, because both FPI signals (A and B) are obtained at nearly the same wavelength range. Radiative transfer calculations remain necessary to assess and possibly correct other error sources fully.

3.2 Ozone interference

Changes in the solar zenith angle (SZA) between background and plume measurement induce changes in the light path of solar radiation through the stratospheric ozone layer. The absorption cross section of ozone drastically increases towards shorter UV wavelengths in the observed spectral range (Fig. 1d). A changing background ozone column therefore will affect the above-described SO_2 measurement principles.

The results of the model calculations are shown in Fig. 5b, where two curves are again plotted for the three measurement setups. The solid lines again show the AA caused only by SO_2 absorption. The dashed lines represent the AA with an additional change in the ozone column density of $\Delta S_{O_3} = 100$ DU. This could for instance be caused by a change in the SZA from 30 to 48° in a 340 DU atmosphere, occurring between the measurement and the last reference measurement.

The simulation again demonstrates that the AA of the SO_2 cameras is much more strongly influenced by changes in the ozone background than the AA_{FPI} of the FPI device. The relative deviations of AA for $S_{SO_2} = 10^{18}$ molec cm^{-2} are $\frac{\Delta AA_{O_3}}{AA} \approx 110\,\%$ for both SO_2 camera implementations. The FPI device shows a significantly smaller deviation throughout the observed S_{SO_2} range. While for lower S_{SO_2}, AA_{FPI} is slightly overestimated ($\frac{\Delta AA_{FPI,\,O_3}}{AA_{FPI}} \approx 3\,\%$ for $S_{SO_2} = 10^{18}$ molec cm^{-2}), saturation at wavelengths of strong SO_2 absorption bands, and therefore flattening of the calibration curve, occurs earlier.

4 FPI camera implementation

4.1 Scanning OP FPI camera

One possible way to obtain 2-D S_{SO_2} distributions is by scanning an FOV with an OP FPI device, similar to scanning DOAS devices (e.g., whisk-broom imaging DOAS). A possible setup for such an OP FPI instrument is proposed in Fig. 6a. The FPI is implemented by two plane-parallel fused silica plates with reflective coatings at the inner surfaces. The separation d of the two plates is tunable by piezo actuators. The outer surfaces either carry anti-reflective coatings or are slightly tilted against each other to avoid additional interference effects. Lens 1, lens 2 and the aperture are chosen so

Table 2. Comparision of the OP FPI camera and a spectrometer used in DOAS measurements (Ocean Optics© USB 2000+), when observing the same spectral range: the surface area A_{lim} and the solid angle Ω_{lim} limiting the etendue $E_{\max}$ mainly contribute to the 6–9 times higher SNR of the OP FPI camera.

		OP FPI device	Spectrometer (DOAS)
	A_{lim}	$314\,\text{mm}^2$	$0.05\,\text{mm}^2$
	Ω_{lim}	3.1×10^{-3} sr	49×10^{-3} sr
	$A_{\text{lim}} \times \Omega_{\text{lim}}$	$973 \times 10^{-3}\,\text{mm}^2$ sr	$2.4 \times 10^{-3}\,\text{mm}^2$ sr
Rel.	$E_{\max}$	400	1
	η	0.2	0.5
	N_I^{-1}	0.25–0.5	1
	$\frac{I^*_{\text{FPI}}}{I^*_{\text{spec}}}$	40–80	
	$\sqrt{\frac{I^*_{\text{FPI}}}{I^*_{\text{spec}}}} \approx \frac{\text{SNR}_{\text{FPI}}}{\text{SNR}_{\text{spec}}}$	6–9	

that for a given aperture angle $(2 \cdot \beta)$, the restriction $\alpha < \alpha_{\max}$ holds for all beams arriving at the FPI. In such a setup, the maximum possible etendue[1] $E_{\max}$ is determined by $\alpha_{\max}$ and the illuminated FPI surface area.

In Table 2, the suggested OP FPI setup is compared to a spectrometer commonly used in volcanic applications (Ocean Optics© USB 2000+) regarding the SNR (note that a telescope usually used with the spectrometer does not reduce the etendue, if well designed). In order to do this, the relative radiances I^*_{FPI} and I^*_{spec} arriving at the detector of the respective instrument were estimated. Relative values of the maximum possible etendue $E_{\max}$ (normalized to the spectrometer etendue) and a loss factor η were taken into account. In addition, the relative radiances have to be divided by the number N_I of radiance measurements needed to obtain one measurement of S_{SO_2}. For the OP FPI device, N_I^{-1} can not exceed 0.5, since at least two radiance measurements (for settings A and B) are needed. Depending on how often a reference measurement (two additional radiance measurements) is recorded, we find $N_I^{-1} \in [0.25, 0.5]$. For the spectrometer, $N_I = 1$, and a factor of $\eta = 0.5$ accounts for losses at the grating. A factor of $\eta = 0.2$ was assumed to account for FPI reflection and absorption. Other losses due to the employed optics were set to unity.

We assumed the FPI to be illuminated on a surface area of 20 mm in diameter (e.g., $R_2 \approx 10$ mm) and with $\alpha_{\max} = 1.8°$, which for an aperture angle of $2 \cdot \beta = 1°$ would require a radius $R_1 = 36$ mm of lens 1. For the USB 2000+, the limiting factors are the $f/4$ optics of the spectrometer and the commonly chosen 1 mm × 50 µm entrance slit (assuming that the cylinder lens option in front of the detector is used, which focuses radiation from the complete height of the slit onto the detector). $E_{\max}$ is then approximated by the product of the limiting surface area A_{lim} and the limiting solid angle Ω_{lim}.

For a measurement in the same spectral range, the relative SNR would be proportional to $\sqrt{\frac{I^*_{\text{FPI}}}{I^*_{\text{spec}}}}$. According to our estimate, the SNR of the OP FPI device is about 6–9 times higher. Thus, with the same SNR, a 40–80 times higher temporal resolution (or associated spatial resolution) can be

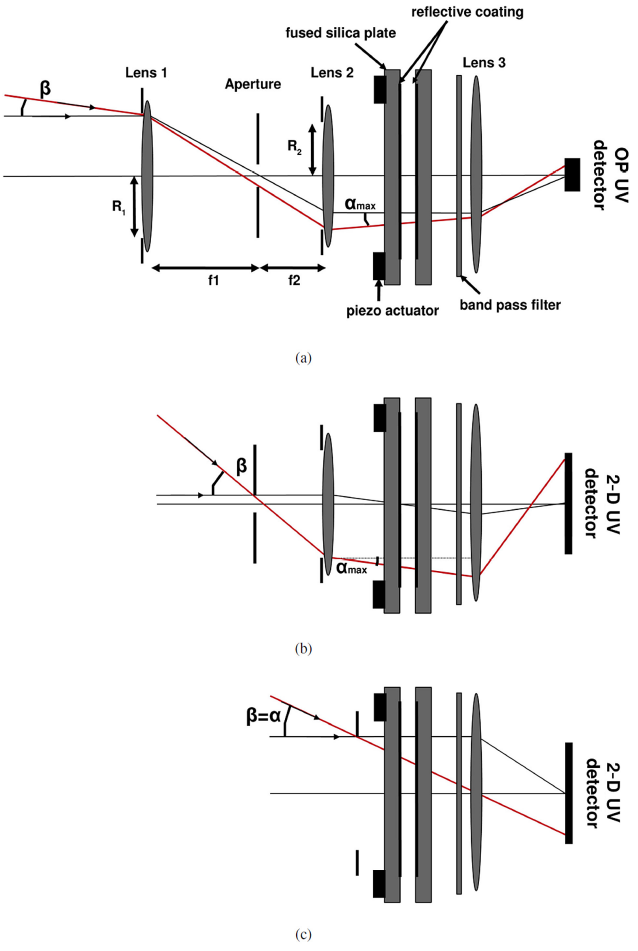

Figure 6. Three possible implementations of an FPI camera. In each setup, the FPI is implemented by two fused silica plates with reflective coatings (reflectivity R) at the inner surfaces, whose separation d is tunable by piezo actuators. The outer surfaces either carry anti-reflective coating or are slightly tilted against each other to exclude additional interference effects. **(a)** One-pixel FPI instrument: two lenses (lens 1, lens 2) and an aperture determine the aperture angle $(2 \cdot \beta)$ of the instrument, constrained by $\alpha_{\max}$. Lens 3 projects the radiation onto a UV-sensitive OP detector after having passed the band-pass filter. 2-D data are achieved by scanning, either by additional optics or by tilting the whole device. **(b)** 2-D FPI camera, where radiation from FOV is parallelized before being projected onto a 2-D detector. **(c)** 2-D FPI camera, where radiation from FOV traverses the FPI under $\alpha = \beta$ for FOV$\approx 20°$. More than two FPI settings are required to obtain non-vanishing sensitivity throughout the FOV (see Fig. 7).

[1]The etendue of an optical instrument is a measure of its maximum possible light throughput, and is defined as the product of the limiting beam solid angle and the receiving area.

reached compared to a DOAS measurement. Of course, the improved etendue of the FPI instrument can be used to obtain a combination of higher SNR (lower detection limit) and higher temporal resolution.

4.2 The 2-D FPI camera

While the use of an FPI in an OP detector has potentially large advantages over conventional spectrometers, the FPI technique can also readily be used as a 2-D detector, just like a SO_2 camera. In the following, two possible 2-D FPI SO_2 camera setups are briefly introduced.

4.2.1 FPI in a parallelized radiation setup

Figure 6b shows a 2-D FPI camera setup. Basically, the implementation is similar to that of the OP FPI device. However, lens 1 is removed to increase the field of view to FOV $\approx 2 \cdot \beta = 2 \cdot \arctan \frac{R_2}{f_2}$, and the OP UV detector is replaced by a UV-sensitive 2-D detector. The radiation from the FOV traverses the FPI parallelized ($\alpha < \alpha_{\max}$) in order to avoid the dependence of AA_{FPI} on β. Evidently, the etendue per pixel is thereby drastically reduced compared to the OP FPI instrument.

This setup (with band-pass interference filters instead of the FPI) was already employed for an SO_2 camera by Kern et al. (2010b), with a comparable entrance aperture (i.e., maximum incidence angle on the filters $\approx \alpha_{\max}$) and, thus, comparable etendue. However, for an FPI SO_2 camera, the radiance reaching the detector is a factor of $\sim$ 30–50 smaller (due to FPI reflection and the measurement at shorter wavelengths; see Fig. 1). Even though the sensitivity of the FPI camera is a factor of ~ 2 higher (see Fig. 5), the SNR would be distinctly lower. Nevertheless, reduced interference with plume AOD and ozone background variation (see Sect. 3) may outweigh a reduced SNR (higher accuracy at lower precision).

4.2.2 High etendue vs. sensitivity structure

Another implementation of a 2-D FPI camera achieving much higher light throughput is depicted in Fig. 6c. The FPI and the band-pass filter are mounted in front of a lens (lens 3), similar to the SO_2 camera setup of, e.g., Mori and Burton (2006). For an FOV $\approx 20°$, the etendue is thereby increased by a factor of about 32 compared to the setup described in Sect. 4.2.1, because the radiation is not parallelized anymore. The maximum incident angle α on the FPI is now determined by the angle $\beta = \frac{\text{FOV}}{2}$. Each detector pixel observes a small, comparable set of incident angles α. However, for a measurement involving two FPI surface separations, the large range of incident angles $\alpha \in [0°, 10°]$ leads to rings of equal, partly vanishing SO_2 sensitivity on the 2-D detector (see Figs. 4 and 7b). To obtain a more or less constant SO_2 sensitivity for the entire FOV (for the entire detector surface), a measurement has to employ more than two

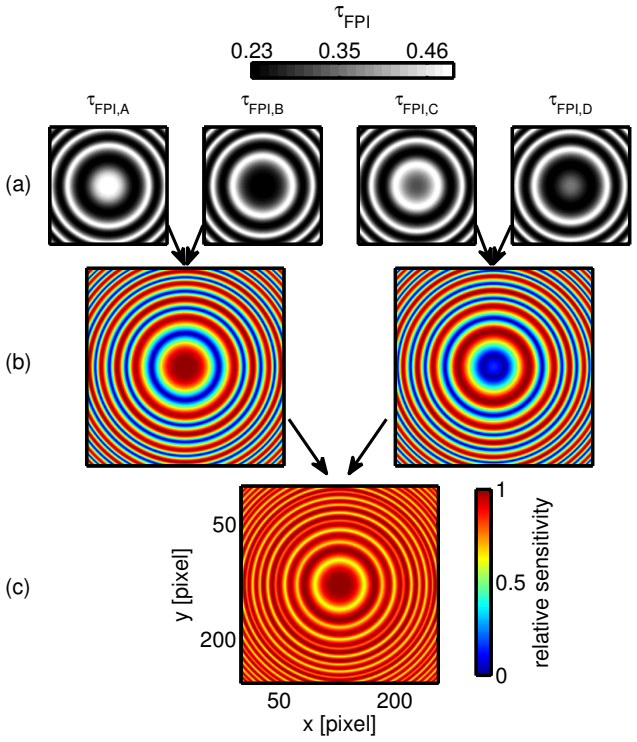

Figure 7. To obtain non-vanishing sensitivity throughout the entire FOV, the FPI camera setup shown in Fig. 6c requires more than two measurement settings. **(a)** Distribution of τ_{FPI} on a 2-D detector for FOV $\approx 20°$ and two different FPI surface separation pairs (d_A and $d_B = d_A + d_{AB}$, $d_C = d_A + \frac{1}{2}d_{AB}$ and $d_D = d_A + \frac{3}{2}d_{AB}$). A homogeneous S_{SO_2} distribution of 10^{18} molec cm^{-2} was assumed. **(b)** Relative sensitivity distributions calculated for each of the d pairs with rings of vanishing sensitivity (blue) at different radii from the detector center. **(c)** Combining the distributions of **(b)** yields non-vanishing sensitivity throughout the entire FOV. By increasing the number of measurements with different FPI settings, the sensitivity distribution on the detector can be smoothed further.

FPI settings (e.g., more than two FPI surface separations d). Figure 7 shows how employing a set of measurements with four different values of the FPI surface separation d arranged into two pairs (d_A and $d_B = d_A + d_{AB}$, $d_C = d_A + \frac{1}{2}d_{AB}$ and $d_D = d_A + \frac{3}{2}d_{AB}$) leads to an SO_2 sensitivity varying by only about 32 % across the entire FOV. By increasing the number of measurements with different FPI settings, the sensitivity distribution on the 2-D detector can be smoothed further.

5 Conclusions

We proposed a remote sensing method to measure volcanic gas emissions using their regular absorption features in the UV wavelength region. The advantage of the Fabry–Perot interferometer used in this method is that its spectral transmittance can be tuned to match precisely the absorption bands of the trace gas of interest. In our theoretical considerations,

parameters of the FPI were specified for SO_2, and possible implementations of measurement setups were discussed.

We presented model calculations and compared the FPI method with the interference filter-based SO_2 camera method. The FPI method exhibits a 1.3–2.5 times higher SO_2 sensitivity. Moreover, a far higher measurement accuracy due to reduced dependence on radiative transfer is reached. For instance, at $S_{SO_2} = 10^{18}$ molec cm^{-2}, the deviations of the AA of SO_2 cameras were 38–54 % for a low plume AOD of approximately 1 and 110 % for an ozone background change of $\Delta S_{O_3} = 100$ DU. In comparison, AA_{FPI} deviated by only < 1 and 3 %, respectively.

As a one-pixel application, the introduced FPI technique has a higher radiation throughput compared to a common miniature spectrometer, while being of comparable size and weight. Thus, a better SNR is obtained and/or much faster measurements are feasible, while the selectivity and immunity to plume AOD and ozone background interferences are still quite good.

Three different imaging implementations were introduced. The first method is based on the whisk-broom imaging approach using an OP FPI device. The second implementation uses an optical system that ensures perpendicular illumination of the FPI. In a third approach, a higher radiation throughput is reached by allowing a larger aperture, leading to a non-perpendicular FPI illumination. The resulting variations of the sensitivity across the detector can be partly overcome by using more than two FPI settings.

Besides SO_2, the technique discussed in this paper can potentially be applied to study other gases with regularly spaced narrow-band absorption in the UV–VIS – like, e.g., BrO, OClO, or IO.

Acknowledgements. We would like to thank the editor Murray Hamilton, the reviewer Robin Campion and an anonymous reviewer whose comments greatly helped to improve the manuscript. We acknowledge financial support by the Deutsche Forschungsgemeinschaft and the Ruprecht-Karls-Universität Heidelberg within the Open Access Publishing funding program.

Edited by: M. Hamilton

References

Barrett, J. J. and Myers, S. A.: New interferometric method for studying periodic spectra using a Fabry–Perot interferometer, J. Opt. Soc. Am., 61, 1246–1251, 1971.

Beirle, S., Hörmann, C., Penning de Vries, M., Dörner, S., Kern, C., and Wagner, T.: Estimating the volcanic emission rate and atmospheric lifetime of SO_2 from space: a case study for Kīlauea volcano, Hawai'i, Atmos. Chem. Phys., 14, 8309–8322, doi:10.5194/acp-14-8309-2014, 2014.

Bluth, G., Shannon, J., Watson, I., Prata, A., and Realmuto, V.: Development of an ultra-violet digital camera for volcanic SO_2 imaging, J. Volcanol. Geoth. Res., 161, 47–56, 2007.

Bobrowski, N., Hönninger, G., Lohberger, F., and Platt, U.: IDOAS: a new monitoring technique to study the 2-D distribution of volcanic gas emissions, J. Volcanol. Geoth. Res., 150, 329–338, 2006.

Bogumil, K., Orphal, J., Homann, T., Voigt, S., Spietz, P., Fleischmann, O., Vogel, A., Hartmann, M., Bovensmann, H., Frerick, J., and Burrows, J.: Measurements of molecular absorption spectra with the SCIAMACHY pre-flight model: instrument characterization and reference data for atmospheric remote sensing in the 230–2380 nm region, J. Photochem. Photobiol. A, 157, 167–184, 2003.

Galle, B., Johansson, M., Rivera, C., Zhang, Y., Kihlman, M., Kern, C., Lehmann, T., Platt, U., Arellano, S., and Hidalgo, S.: Network for Observation of Volcanic and Atmospheric Change (NOVAC) – A global network for volcanic gas monitoring: network layout and instrument description, J. Geophys. Res. D, 115, D05304, doi:10.1029/2009JD011823, 2010.

Hönninger, G., von Friedeburg, C., and Platt, U.: Multi axis differential optical absorption spectroscopy (MAX-DOAS), Atmos. Chem. Phys., 4, 231–254, doi:10.5194/acp-4-231-2004, 2004.

Kern, C., Deutschmann, T., Vogel, L., Wöhrbach, M., Wagner, T., and Platt, U.: Radiative transfer corrections for accurate spectroscopic measurements of volcanic gas emissions, B. Vulcanol., 72, 233–247, 2010a.

Kern, C., Kick, F., Lübcke, P., Vogel, L., Wöhrbach, M., and Platt, U.: Theoretical description of functionality, applications, and limitations of SO_2 cameras for the remote sensing of volcanic plumes, Atmos. Meas. Tech., 3, 733–749, doi:10.5194/amt-3-733-2010, 2010b.

Kern, C., Werner, C., Elias, T., Sutton, A. J., and Lübcke, P.: Applying UV cameras for SO_2 detection to distant or optically thick volcanic plumes, J. Volcanol. Geoth. Res., 262, 80–89, 2013.

Louban, I., Bobrowski, N., Rouwet, D., Inguaggiato, S., and Platt, U.: Imaging DOAS for volcanological applications, B. Volcanol., 71, 753–765, 2009.

Lübcke, P., Bobrowski, N., Illing, S., Kern, C., Alvarez Nieves, J. M., Vogel, L., Zielcke, J., Delgado Granados, H., and Platt, U.: On the absolute calibration of SO_2 cameras, Atmos. Meas. Tech., 6, 677–696, doi:10.5194/amt-6-677-2013, 2013.

McGonigle, A. J. S., Delmelle, P., Oppenheimer, C., Tsanev, V. I., Delfosse, T., Williams-Jones, G., Horton, K., and Mather, T. A.: SO_2 depletion in tropospheric volcanic plumes, Geophys. Res. Lett., 31, L13201, doi:10.1029/2004GL019990, 2004.

Millan, M. M.: Remote sensing of air pollutants, A study of some atmospheric scattering effects, Atmos. Environ., 14, 1241–1253, 1980.

Millan, M. M.: Aborption correlation spectroscopy, in: The COSPEC Cookbook: Making SO_2 measurements at active volcanoes, edited by: Williams-Jones, G., Stix, J., and Hickson, C., IAVCEI, Methods in Volcanology, 1, 1–62, 2008.

Moffat, A. J. and Millan, M. M.: The applications of optical correlation techniques to the remote sensing of SO_2 plumes using sky light, Atmos. Environ., 5, 677–690, 1971.

Mori, T. and Burton, M.: The SO_2 camera: A simple, fast and cheap method for ground-based imaging of SO_2 in volcanic plumes, Geophys. Res. Lett., 33, L24804, doi:10.1029/2006GL027916, 2006.

Nadeau, P. A., Palma, J. L., and Waite, G. P.: Linking volcanic tremor, degassing, and eruption dynamics via SO_2 imaging, Geophys. Res. Lett., 38, L01304, doi:10.1029/2010GL045820, 2011.

Perot, A. and Fabry, C.: On the application of interference phenomena to the solution of various problems of specrtoscopy and metrology, Astrophys. J., 9, 87–115, 1899.

Platt, U. and Stutz, J.: Differential Optical Absorption Spectroscopy: Principles and Applications (Physics of Earth and Space Environments), Springer, 2008.

Spinetti, C. and Buongiorno, M.: Vulcanic aerosol optical characteristics of Mt. Etna tropospheric plume retrieved by means of airborne multispectral images, J. Atmos. Sol.-Terr. Phy., 69, 981–994, 2007.

Textor, C., Graf, H., Timmreck, C., and Robock, A.: Emissions from volcanoes, in: Emissions of Atmospheric Trace Gas Compounds, Kluwer, Dordrecht, 296–303, 2004.

Vargas-Rodriguez, E. and Rutt, H. N.: Design of CO, CO_2 and CH_4 gas sensors based on correlation spectroscopy using a Fabry–Perot interferometer, Sensor Actuat. B-Chem., 137, 410–419, 2009.

von Glasow, R., Bobrowski, N., and Kern, C.: The effects of volcanic eruptions on atmospheric chemistry, Chem. Geol., 263, 131–142, 2008.

Wilson, E. L., Georgieva, E. M., and Heaps, W. S.: Development of a Fabry–Perot interferometer for ultra-precise measurements of column CO_2, Meas. Sci. Technol., 18, 1495–1502, 2007.